Slow-Light Frequency Combs and Dissipative Kerr Solitons in Coupled-Cavity Waveguides

J.P. Vasco* and V. Savona

Institute of Theoretical Physics, École Polytechnique Fédérale de Lausanne EPFL, CH-1015 Lausanne, Switzerland

(Received 25 July 2019; revised manuscript received 28 October 2019; published 31 December 2019)

We study Kerr frequency combs and dissipative Kerr solitons in silicon photonic crystal coupled-cavity waveguides (CCWs) with globally optimized dispersion at telecom wavelengths. The corresponding threshold for comb generation is found to explicitly depend on the main CCW figures of merit, namely, the mode volume, the normal-mode quality factor, and the slow-light group index. Our analysis is carried out by solving the nonlinear dynamics of the CCW Bloch modes in the presence of Kerr nonlinearity and two-photon absorption. Our results open the way to CCW comb generation via dispersion engineering and slow-light enhancement.

DOI: 10.1103/PhysRevApplied.12.064065

I. INTRODUCTION

Kerr frequency combs have revolutionized several fields in optical sciences since they were first proposed in monolithic microresonators [1]. To date, they have been successfully applied to a vast variety of state-of-the-art technologies and highly sophisticated measurement techniques such as ultrahigh-resolution spectroscopy [2,3], massively parallel coherent optical communications [4], light detection and ranging (LIDAR) [5], optical-frequency synthesizers [6], and microphotonic astrocombs [7,8]. Frequency combs in optical microresonators are generated by the interaction of either a continuous-wave (cw) pump laser or pumped optical pulses [9], with the resonator modes via parametric four-wave mixing (FWM), assisted by the Kerr nonlinearity of the material. This parametric process fulfills energy conservation and is enhanced when the side bands created by the FWM coincide with the resonator frequencies. Since the intensity-dependent refractive index induces a frequency shift on the modes, an increasing free spectral range (FSR) with frequency (anomalous dispersion) is required to compensate this effect and effectively produce equidistant spectral lines suitable to support the cascaded FWM [10]. When a high number of mode-locked modes are involved in this nonlinear interaction and dissipation cannot be neglected, the complex nonlinear dynamics may give rise to dissipative Kerr solitons (DKSs), which arise as a double balance between nonlinearity and dispersion (preserving their shape), as well as dissipation and parametric gain (preserving their amplitude) [11]. Moreover, multiple-soliton formations have become very interesting in the context of localized-state interactions [12–14], breather solitons [15–17], and soliton crystals [18,19]. DKSs are notably relevant because their corresponding spectra exhibit highly coherent frequency combs with perfect single-FSR spacing between side bands [20,21] and dispersive waves in the presence of high-order dispersion [22–25]. The latter is particularly important because it allows a further spanning of the frequency combs, highlighting the important role of dispersion engineering on parametric gain and, consequently, on comb generation [26]. Such a task has been successfully achieved in nonlinear microresonators by varying the ring geometrical parameters in order to tailor the dispersion for specific comb functionalities [27–29]. Nevertheless, this geometry has a limited parameter space, thus restricting the choice of materials, the operation wavelength, and the size of the final device. Recently, Fabry-Perot resonators have been proposed as appealing candidates for frequency-comb generation since different methods to reshape the cavity dispersion can be applied [30,31]; however, advanced dispersion engineering still remains challenging.

In this work, we propose a coupled-cavity waveguide (CCW, also known as a coupled-resonator optical waveguide or CROW) as an alternative candidate to efficiently generate low-threshold Kerr frequency combs and DKSs. Similar to ring resonators, CCWs define a discrete spectrum of propagating modes that may trigger cascaded parametric FWM in the anomalous dispersion regime and lead to a highly coherent comb if the waveguide dispersion is conveniently optimized. In fact, since their appearance two decades ago [32], CCWs have been shown to be extremely flexible for advanced dispersion engineering

*juan.vasco@epfl.ch

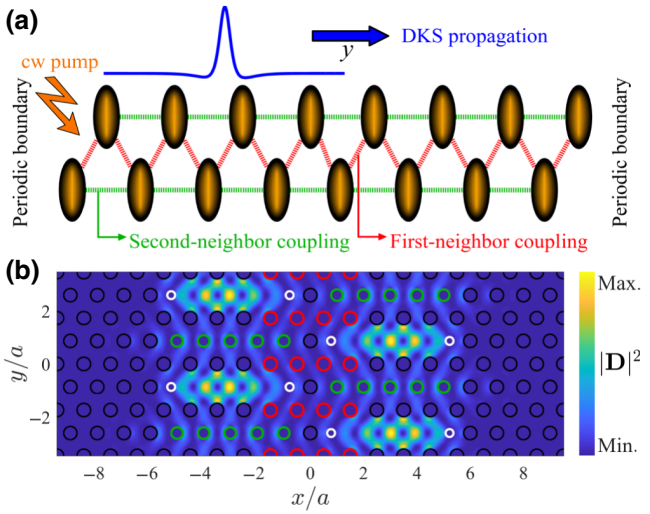

FIG. 1. (a) A schematic representation of a CCW system with first- and second-neighbor cavity coupling. The system is pumped with a cw source and a DKS propagates along the waveguide y direction. (b) A photonic crystal CCW formed by coupled L3 cavities, where the red and green holes are allowed to vary in size to tune the first- and second-neighbor coupling, respectively, while the out-of-plane losses of the waveguide Bloch modes are optimized by varying the position and size of the white holes. The intensity profile of the displacement field $[\mathbf{D}(\mathbf{r}) = \epsilon(\mathbf{r})\vec{\mathcal{E}}(\mathbf{r})]$ is shown at the boundary of the Brillouin zone.

and enhancement of nonlinear phenomena via slow light [33–38]. We show in Fig. 1(a) a schematic representation of the CCW studied in this work. The periodic waveguide is formed by a staggered distribution of cavities where first- (dashed red) and second- (dashed green) neighbor cavity-cavity coupling is assumed. The system is pumped with a cw source and a DKS is propagating along the waveguide y direction.

II. NONLINEAR PHOTONIC CRYSTAL CCW

The system of Fig. 1(a) is realized with the waveguide of coupled L3 photonic crystal slab cavities shown in Fig. 1(b), where we have plotted the intensity profile of the displacement field $[\mathbf{D}(\mathbf{r}) = \epsilon(\mathbf{r})\vec{\mathcal{E}}(\mathbf{r})]$ at the boundary of the Brillouin zone. The photonic crystal is formed by a hexagonal lattice of holes of pitch $a = 400$ nm and hole radius $r = 0.25a$, etched in a silicon membrane of thickness $d = 0.55a$, and the L3 cavity is introduced by removing three holes along the ΓK direction of the lattice. This CCW configuration allows us to tune the first- and second-neighbor coupling between the L3 cavities by varying the size of the red and green holes, respectively, and to optimize the out-of-plane losses by varying the position and size of the white ones. The waveguide of Fig. 1(b) has been previously proposed as a compact CCW with outstanding figures of merit obtained via automated global optimization [38] and successfully measured experimentally [39,40]. Here, we adopt the design with largest averaged group index and small second-order dispersion reported in Ref. [38], with parameters $(\Delta r_1, \Delta r_2, \Delta r_3, \Delta x) = (-0.0049, -0.0340, -0.1016, 0.2204)a$, where $r_1 = r + \Delta r_1$, $r_2 = r + \Delta r_2$, and $r_3 = r + \Delta r_3$ are the radii of the red, green, and white holes, respectively, and Δx is the outward displacement of the white holes. The dispersion relation ν_α of the waveguide and the decay rates γ_α of the Bloch modes of momentum α are calculated using the guided-mode-expansion (GME) method [41] for a system length of $M = 400$ cavities (400 normal modes within the Brillouin zone of the CCW) with period $l = \sqrt{3}a$ (waveguide length $L = Ml$), while the nonlinear mode volume is computed using a commercial finite-difference time-domain solver [42] and is found to be $V_c = 0.345\ \mu\text{m}^3$. This sample length represents a good compromise between the total number of normal modes (avoiding finite-size effects in the coupled-mode equations (A3)) and robustness to fabrication disorder [40,43]. Silicon parameters at telecom frequencies are considered for the material, namely, the dielectric constant $\epsilon = 12.04$, the Kerr coefficient $n_2 = 5.52 \times 10^{-18}\ \text{m}^2/\text{W}$, and the two-photon absorption (TPA) coefficient $\beta_{\text{TPA}} = 1 \times 10^{-11}\ \text{m/W}$ [44]. The GME dispersion relation, second-order dispersion, and group index are shown in Figs. 2(a)–2(c), respectively, for which the red and blue segments correspondingly highlight the regions of normal and anomalous dispersion. Note that these dispersion curves are valid for a straight waveguide with periodic boundary conditions; nevertheless, we expect them to describe very well a closed loop of coupled cavities as bending losses is usually very small, with respect to out-of-plane losses, in photonic crystal geometries [45]. The system is pumped at $a\alpha_0 = 1.2742$, where $\nu_{\alpha_0} = 193.39$ THz, $(ac)^{-1}(d^2\nu/\alpha^2)_{\alpha_0} = 8.63 \times 10^{-4}$, $n_{g,\alpha_0} = 119.34$, and the normal-mode quality factor is $Q_{\alpha_0} = 5.72 \times 10^4$. This sets an internal-mode threshold given by (see Appendix A)

$$|\mathcal{A}_{\alpha_0}|^2_{\text{th}} = \frac{\epsilon V_c}{2ln_{g,\alpha_0}n_2Q_{\alpha_0}} f(\kappa) = 138\ \text{mW}, \qquad (1)$$

where $\mathcal{A}_{\alpha_0}$ is the slowly varying amplitude of the Bloch mode α_0 and $f(\kappa) = (\sqrt{1+\kappa^2} + 2\kappa)/(1 - 3\kappa^2)$, with $\kappa = c\beta_{\text{TPA}}/(2n_2\omega_{\alpha_0})$, is a function of the material parameters only, which gives $f(\kappa = 0.2236) = 1.73$ for silicon at $\omega_{\alpha_0}/2\pi = \nu_{\alpha_0} = 193.39$ THz and reduces to $f(\kappa = 0) = 1$ for $\beta_{\text{TPA}} = 0$. This result is particularly remarkable because, even considering that TPA increases the threshold by a factor of 1.73, $|\mathcal{A}_{\alpha_0}|^2_{\text{th}} = 138$ mW is still one order of magnitude smaller than in typical millimeter-size crystalline nonlinear ring resonators [46]. Equation (1) undoubtedly strengthens the potential capabilities of CCW

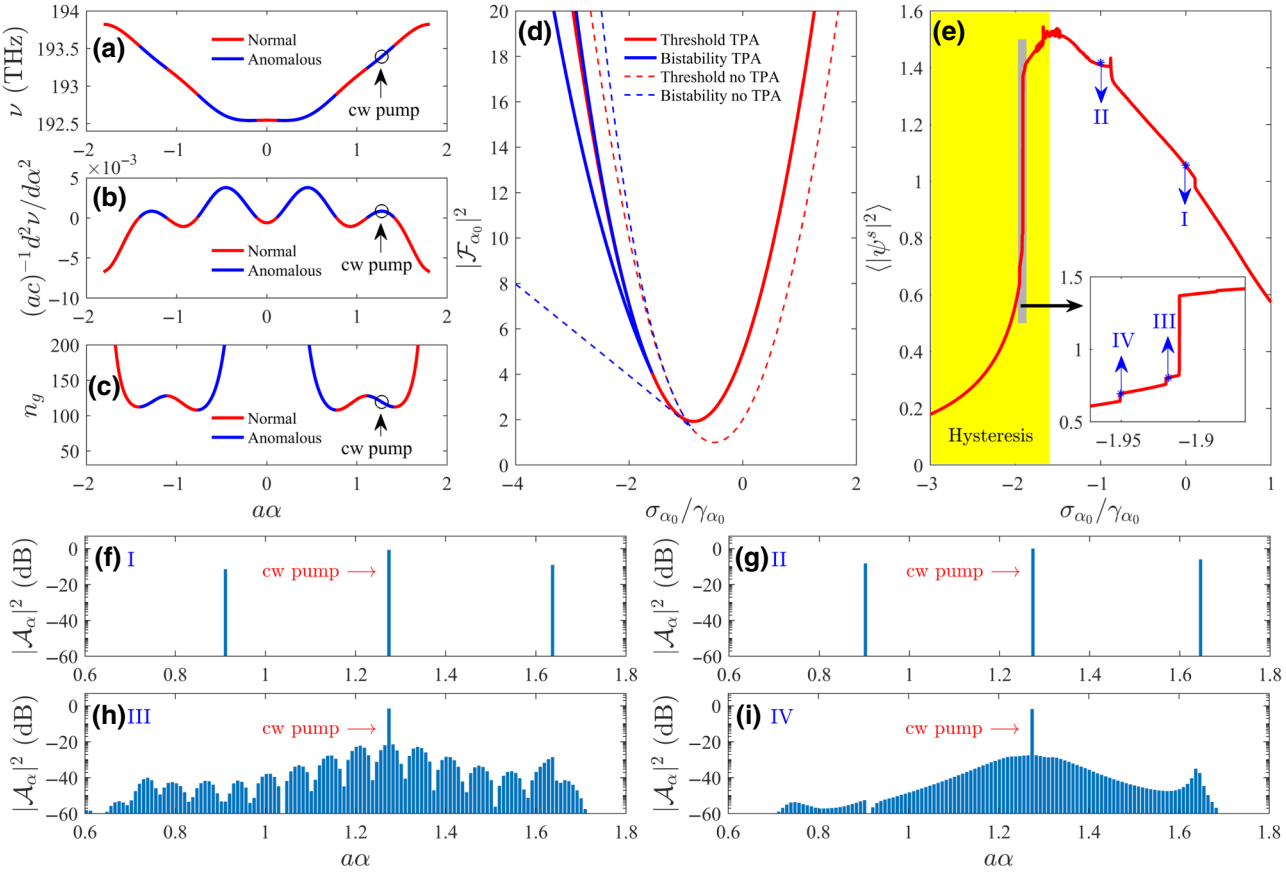

FIG. 2. The dispersion relation (a), second-order dispersion (b), and group index (c) in the Brillouin zone of a photonic crystal CCW of 400 L3 cavities. The red and blue curves are where the dispersion is normal and anomalous, respectively. The waveguide is pumped at $a\alpha_0 = 1.2742$. (d) The threshold (red curve) and bistability boundaries (blue curves) determined by the external pump intensity $|\mathcal{F}_{\alpha_0}|^2$ as a function of the laser detuning σ_{α_0}. The dashed curves are for $\beta_{\mathrm{TPA}} = 0$. (e) The averaged intrawaveguide power of the CCW in the steady state as a function of σ_{α_0} for $|\mathcal{F}_{\alpha_0}|^2 = 6|\mathcal{A}_{\alpha_0}|^2_{\mathrm{th}}$. Hysteresis arises in the yellow region $\sigma_{\alpha_0} < -\gamma_{\alpha_0}\sqrt{3}\rho(\kappa)/2$ with $\rho(\kappa = 0.2236) = 1.84$ (see Appendix B): the inset corresponds to an enlargement of the rectangular gray area where the discrete steps, the signature of switching between soliton states, appear. The corresponding frequency combs at the points marked I–IV in (e) are, respectively, shown in (f) the supercritical Turing pattern of the 40-FSR (355.2-GHz) repetition rate, (g) the supercritical Turing pattern of the 41-FSR (363.3-GHz) repetition rate, (h) the soliton molecule of two pulses with a single-FSR (9.1-GHz) repetition rate, and (i) the soliton pulse with a single-FSR repetition rate. All power quantities are given in decibel units relative to the threshold $|\mathcal{A}_{\alpha_0}|^2_{\mathrm{th}}$, while the detunings are in γ_{α_0} units.

structures for low-threshold comb generation. While the factor V/Q also enters in the expression for the internal-mode threshold of ring resonators [47–49], CCWs can drastically decrease this minimal power in the slow-light regime, i.e., for $n_{g,\alpha_0} \gg \sqrt{\epsilon}$. Such a structural effect allows us to access the rich physics of DKSs in CCWs at much lower powers than in their monolithic counterparts, even in the presence of strong TPA, which is the main source of nonlinear losses in silicon structures at telecom wavelengths [50,51]. It is worth emphasizing that since we are not specifying any particular coupling architecture with the external pump, we are referring to the internal-mode threshold, which scales as $1/Q$, and not to the external-power threshold, which is found to scale as $1/Q^2$ for ring resonators at critical coupling with the external source [52]. While the latter is an important parameter to set the excitation power in an experimental setup, the former quantity, also called the minimum intracavity power for comb generation [46], gives the corresponding effective power into the specific normal mode of the system. In Fig. 2(d), we plot the driven intensity $|\mathcal{F}_{\alpha_0}|^2$ [Eq. (B1) in Appendix B], in $|\mathcal{A}_{\alpha_0}|^2_{\mathrm{th}}$ units, evaluated at threshold (continuous red lines) and at the bistability boundaries (continuous blue curves), as a function of the laser detuning $\sigma_{\alpha_0} = \Omega_0 - \omega_{\alpha_0}$ in units of γ_{α_0}, where the dashed lines are the corresponding curves for $\beta_{\mathrm{TPA}} = 0$. The effects of TPA on the threshold are clearly seen in this plot; moreover, the hysteresis region (where the system has bistable states) is red shifted and the area between the bistability boundaries is significantly reduced. Hence, the system

needs to be pumped more strongly and the laser frequency has to be further decreased to see Kerr frequency combs and DKSs in the presence of TPA.

III. FREQUENCY-COMB AND DKS SOLUTIONS

In order to find the possible steady state solutions determined by the nonlinear CCW dynamics, we carry out a frequency scan at $|\mathcal{F}_{\alpha_0}|^2 = 6|\mathcal{A}_{\alpha_0}|^2_{\rm th}$ in Fig. 2(d) within the $\sigma_{\alpha_0}/\gamma_{\alpha_0}$ interval $[-3, 1]$. The dynamical nonlinear coupled-mode equations [see Eq. (A3) in Appendix A] are thus propagated in time for each σ_{α_0} value along this trajectory using an explicit Runge-Kutta integrator and fast Fourier transform (see Ref. [53]) until the steady state is reached (see the transient dynamics in Ref. [54]). Our simulation takes into account the momentum-dependent decay rate γ_α of the Bloch modes and the initial condition of the integrator is a sharp Gaussian pulse $\psi(y,0) = \exp[-0.5(y/l)^2]$, where $\psi(y,t) = \sum_\alpha \mathcal{A}_\alpha(t)\, e^{i\sigma_\alpha t}\, e^{-i(\alpha-\alpha_0)y}$ is the envelope function along the CCW direction. The results of this analysis are presented in Fig. 2(e), where we show the averaged waveguide power in the steady state $\langle|\psi^s|^2\rangle = \int_L |\psi^s(y)|^2\, dy$, in units of threshold, as a function of the laser detuning. When the laser frequency is red shifted, the intrawaveguide power starts to increase until a clear series of discrete steps (see the inset), which decrease the average power, are seen in the yellow area, which corresponds to the region in which there is hysteresis in the system and the soliton solutions are expected to appear [11,55]. In fact, these steps have been previously measured experimentally in the transmission of nonlinear ring resonators and they are associated with the formation of different soliton states within the system, in excellent agreement with the predictions of the nonlinear coupled-mode equations and the Lugiato-Lefever formalism [20]. In Figs. 2(f)–2(i), we show the respective frequency combs at the four representative points marked in Fig. 2(e). Figures 2(f) and 2(g) display a sequence of primary combs separated by 40-FSR and 41-FSR, respectively, which correspond to supercritical Turing patterns as they are excited above threshold. In Figs. 2(h) and 2(i), both combs are subcritical (excited right below threshold) with a single FSR spacing and they are the signature of soliton complexes. Notably, because of the presence of nontrivial high-order terms in the dispersion relation of the photonic crystal CCW, these frequency combs have signatures of dispersive-wave formation or soliton Cherenkov radiation at the linear phase-matching condition $\omega_\alpha - [\omega_{\alpha_0} + \zeta_1(\alpha - \alpha_0)] = 0$, where ζ_1 represents the group velocity [25]. In particular, the dispersive peak closest to the zero comb line is predicted to be around $a\alpha \simeq 1.63$, which is in perfect agreement with our numerical simulations. The corresponding steady-state intensities of the envelope functions are shown in Fig. 3. For states I (40 FSR repetition rate) and II (41 FSR repetition rate), we

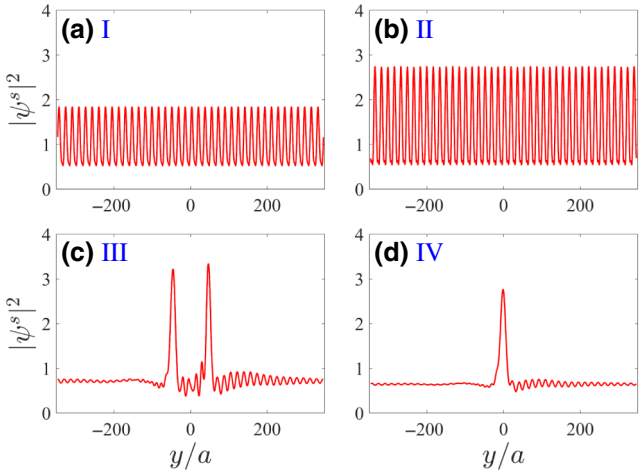

FIG. 3. Steady-state envelope functions at the points marked I–IV in Fig. 2(e). (a) The supercritical Turing pattern with 40 rolls. (b) The supercritical Turing pattern with 41 rolls. (c) The soliton molecule of two pulses. (d) A single-soliton pulse. $|\psi^s|^2$, given in units of the power threshold $|\mathcal{A}_{\alpha_0}|^2_{\rm th}$.

see 40 and 41 Turing rolls, respectively, in agreement with the Lugiato-Lefever theory of Kerr frequency combs in the anomalous dispersion regime [55]. Moreover, for states III and IV we clearly identify, respectively, a soliton molecule composed of two pulses and a single-soliton pulse, propagating along the waveguide direction while keeping their shape and amplitude. It must be said that because these soliton structures are subcritical (pumped below threshold), they are extremely sensitive to the initial conditions and, therefore, the system may follow different trajectories in Fig. 2(e) when slightly changing the Bloch-mode amplitudes at $t = 0$ [20,55]. Furthermore, the characteristic width of the soliton pulse is much smaller than the waveguide length, thus ruling out finite-size effects in the basis expansion. While the results presented in Fig. 2 are strictly valid for a CCW system with periodic boundary conditions, we still expect highly coherent combs in finite waveguides where non-negligible corrections to the nonlinear interaction are predicted by the theory of frequency combs in Fabry-Perot resonators [30]. Nevertheless, a rigorous quantitative analysis is beyond the scope of this paper and will be the focus of future work.

Figure 4 shows the frequency spectrum of the DKS in Fig. 3(d), where the unloaded modes (the normal modes of the CCW) are represented by the vertical dashed lines. As expected from energy conservation, the spectral lines are equally spaced with a repetition rate of 9.1 GHz. Such rates have previously been achieved in nonlinear ring resonators of 7 mm diameter [56], in contrast to our system length of approximately 277 μm. Note that the minimal external power for comb generation may vary significantly, depending on the material, geometry, and, more importantly, the coupling architecture with a bus waveguide [46]; however,

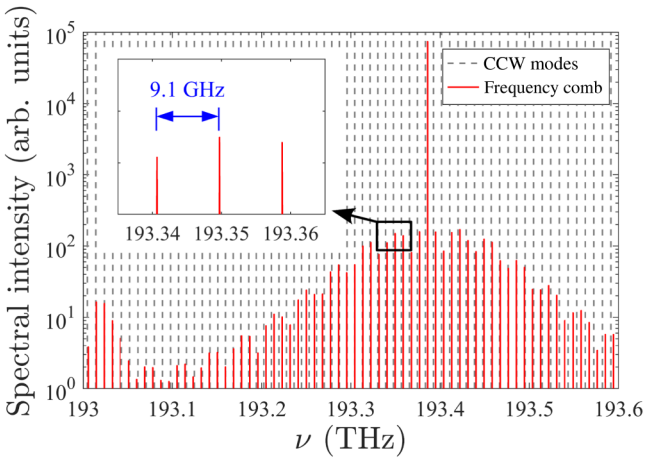

FIG. 4. The frequency spectrum of the DKS in Fig. 3(d), where the dashed vertical lines represent the normal modes of the photonic crystal CCW. A small repetition rate of 9.1 GHz is obtained.

this key result notably highlights the potential capabilities of micrometer-scale low-threshold CCW systems to generate low-rate frequency combs, which are desirable in high-precision comb applications [11].

It is important to stress that the specific choice of photonic crystal CCWs is mainly motivated by their characteristic diffraction-limited mode volumes [57], which play an important role in decreasing the threshold power and the final device size. Nevertheless, the results presented in this section only rely on the dispersion relation of the CCW and are therefore expected to hold for any CCW system, e.g., coupled microrings, displaying anomalous dispersion with, more generally, nth-neighbor coupling.

IV. CONCLUSIONS

In conclusion, we present results on Kerr frequency combs and DKSs in CCWs where the main source of nonlinear loses is given by TPA. We find that the internal-mode threshold for comb generation depends on the main CCW figures of merit, namely, the cavity volume, the normal-mode quality factor, and the group index. While TPA losses have the main effect of increasing the threshold power and inducing a red shift in the optimal laser detuning, structural slow-light plays an important role in reducing the minimal power to trigger FWM phenomena between the CCW normal modes, evidencing the capabilities of CCW systems for low-threshold frequency combs. Specifically, we demonstrate the possibility of DKSs in a realistic dispersion-engineered silicon photonic crystal CCW at telecom wavelengths, where highly complex combs are seen with signatures of soliton Cherenkov radiation. Repetition rates of a few gigahertz in an approximately 277-μm-length photonic crystal CCW are obtained into the soliton regime, which are commonly achieved in approximately 7-mm-size ring resonators, thus demonstrating the potential of CCW systems for high-precision comb applications in ultracompact devices. Finally, although the spectral spanning of the combs generated in CCW is limited to the waveguide bandwidth, our results open the way to Kerr-frequency-comb and DKS generation via advanced dispersion engineering and slow-light nonlinear enhancement.

APPENDIX A: NONLINEAR COUPLED-MODE EQUATIONS

In order to derive a set of coupled-mode equations for the CCW system, we expand the total field inside the waveguide as

$$\mathbf{E}(\mathbf{r},t)=\sqrt{\frac{2l}{\varepsilon_0}}\sum_{\mu}\mathcal{A}_{\mu}(t)\,e^{-i\omega_{\mu}t}\frac{1}{\sqrt{v_{\mu}}}\vec{\mathcal{E}}_{\mu}(\mathbf{r})+E_{\mathrm{ext}}\,e^{-i\Omega_0 t}\hat{e}_0, \tag{A1}$$

where l is the period of the CCW, $\mathcal{A}_{\mu}(t)$ is the slowly varying amplitude of the normal mode $\vec{\mathcal{E}}_{\mu}(\mathbf{r})$ with eigenfrequency ω_{μ} $(2\pi\nu_{\mu})$ and group velocity v_{μ}, and E_{ext} is the external field amplitude of the cw pump with frequency Ω_0, polarized along the $\hat{e}_0$ direction. The expansion of Eq. (A1) is introduced into the nondispersive and isotropic Maxwell's wave equation [58] with a nonlinear dielectric function given by [59]

$$\epsilon(\mathbf{r},|\mathbf{E}|^2)=\epsilon(\mathbf{r})\left\{1+\varepsilon_0 c\left[n_2(\mathbf{r})+i\frac{c}{2\omega_0}\beta_{\mathrm{TPA}}(\mathbf{r})\right]|\mathbf{E}|^2\right\}, \tag{A2}$$

where $n_2(\mathbf{r})$ and $\beta_{\mathrm{TPA}}(\mathbf{r})$ denote the spatially dependent Kerr and TPA coefficients, respectively, and ω_0 is the reference frequency at which n_2 and β_{TPA} are experimentally measured. By explicitly assuming the slowly varying amplitude approximation on $\mathcal{A}_{\mu}$ (which allows us to neglect the second time derivative $\ddot{\mathcal{A}}_{\mu}(t)$ and to keep only the $\mathcal{A}_{\mu}(t)$ terms in the nonlinear contribution), a local Kerr effect at the cavity level, identical single-mode cavities, periodic boundary conditions, and nonlinear strength mainly determined by the frequency at which the nonlinear effect takes place [60], we arrive at the system of coupled-mode equations (see Ref. [54])

$$\begin{aligned}\dot{\mathcal{B}}_{\alpha}(t)=&-\left[\frac{\gamma_{\alpha}}{2}-i\sigma_{\alpha}\right]\mathcal{B}_{\alpha}(t)\\&+iG_{\alpha_0}\sum_{\mu\eta}\mathcal{B}_{\mu}(t)\mathcal{B}^{*}_{\eta}(t)\mathcal{B}_{\alpha+\eta-\mu}(t)+\frac{\gamma_{\alpha}}{2}\mathcal{F}_{\alpha}\delta_{\alpha,\alpha_0},\end{aligned} \tag{A3}$$

where $\gamma_{\alpha}\ll\omega_{\alpha}$ represents the overall losses of the α mode. In Eq. (A3), the explicit time dependence has

been removed by carrying out the transformation $\mathcal{B}_\alpha(t) = \mathcal{A}_\alpha(t)\, e^{i\sigma_\alpha t}$, where the mode detuning, with respect to the laser frequency Ω_0, is defined as $\sigma_\alpha = \Omega_0 - \omega_\alpha$. Moreover, we have introduced the complex gain

$$G_{\alpha_0} = g_{\alpha_0} + i g_{\alpha_0}^{\mathrm{TPA}} = \left(\frac{l\omega_{\alpha_0} n_{g,\alpha_0} n_2}{\epsilon V_c}\right) + i\left(\frac{l c n_{g,\alpha_0}\beta_{\mathrm{TPA}}}{2\epsilon V_c}\right), \tag{A4}$$

where α_0 is the CCW mode resonant with the cw pump, n_{g,α_0} is the group index at ω_{α_0}, ϵ is the dielectric constant of the nonlinear material, and V_c is the nonlinear cavity-mode volume. The drive term of Eq. (A3) reads

$$\mathcal{F}_\alpha = \frac{i\Omega_0^2}{\omega_\alpha \gamma_\alpha}\sqrt{\frac{\varepsilon_0 v_\alpha}{2l}} E_{\mathrm{ext}} \int_l \epsilon(\mathbf{r})\vec{\mathcal{E}}_\alpha^*(\mathbf{r})\cdot\hat{e}_0\, dV, \tag{A5}$$

where L represents the total length of the waveguide, which is equal to Ml for M cavities.

APPENDIX B: STABILITY AND THRESHOLD

The stability analysis of the stationary solutions $\mathcal{B}_\alpha^s$ of Eq. (A3), obtained by setting $\dot{\mathcal{B}}_\alpha(t) = 0$, can be separated into two main regimes: system below threshold and system at threshold. When the system is below threshold, only the pumped mode α_0 is excited and the single amplitude present in the steady state is $\mathcal{B}_{\alpha_0}^s$ (or $\mathcal{A}_{\alpha_0}^s$), which is also called the zero-order comb. Here, the relation between the driven and internal-mode intensities is given by the cubic equation

$$\begin{aligned}|\mathcal{F}_{\alpha_0}|^2 = &\left(1 + \frac{4\sigma_{\alpha_0}^2}{\gamma_{\alpha_0}^2}\right)|\mathcal{B}_{\alpha_0}^s|^2 \\ &+ \frac{4}{\gamma_{\alpha_0}}\left(\frac{2g_{\alpha_0}\sigma_{\alpha_0}}{\gamma_{\alpha_0}} + g_{\alpha_0}^{\mathrm{TPA}}\right)\left[|\mathcal{B}_{\alpha_0}^s|^2\right]^2 \\ &+ \frac{4|G_{\alpha_0}|^2}{\gamma_{\alpha_0}^2}\left[|\mathcal{B}_{\alpha_0}^s|^2\right]^3,\end{aligned} \tag{B1}$$

which displays hysteresis for $\sigma_{\alpha_0} < -\gamma_{\alpha_0}\sqrt{3}\rho(\kappa)/2$, with $\rho(\kappa) = [(4\sqrt{3} + 3\kappa)\kappa + 3]/[3(1 - 3\kappa^2)]$ and $\kappa = g_0^{\mathrm{TPA}}/g_0 = c\beta_{\mathrm{TPA}}/(2n_2\omega_0)$. The bistability boundaries determined by Eq. (B1) are easily found by solving $\partial|\mathcal{F}_{\alpha_0}|^2/\partial|\mathcal{B}_{\alpha_0}^s|^2 = 0$. On the other hand, when the system is at threshold, side modes around $\mathcal{B}_{\alpha_0}^s$ are also excited, thus leading to comb generation. In order to find such a threshold power, we first assume the system to be in the trivial equilibrium, in which $\mathcal{B}_{\alpha_0}^s \neq 0$ and the two pairs of modes fulfill $\mathcal{B}_{\pm\alpha'}^s = 0$, with $\alpha' = \alpha - \alpha_0$. Then, we add a small time-dependent perturbation to this equilibrium state, i.e., $\mathcal{B}_{\alpha'}(t) = \mathcal{B}_{\alpha'}^s\delta_{\alpha',0} + \delta\mathcal{B}_{\alpha'}(t)$, and linearize Eq. (A3) on $\delta\mathcal{B}_{\alpha'}(t)$ (see details in Ref. [54]). The minimum mode power that turns stable solutions of Eq. (A3) into unstable ones, i.e., instability of the trivial equilibrium, defines the internal threshold for the onset of side-mode oscillations and is given (in watts) by

$$|\mathcal{A}_{\alpha_0}|_{\mathrm{th}}^2 = |\mathcal{B}_{\alpha_0}|_{\mathrm{th}}^2 = \frac{\gamma_{\alpha_0}}{2g_{\alpha_0}} f(\kappa) = \frac{\epsilon V_c}{2l n_{g,\alpha_0} n_2 Q_{\alpha_0}} f(\kappa), \tag{B2}$$

where $Q_{\alpha_0} = \omega_{\alpha_0}/\gamma_{\alpha_0}$ is the quality factor of the driven CCW normal mode α_0 and $f(\kappa) = (\sqrt{1+\kappa^2} + 2\kappa)/(1 - 3\kappa^2)$. The function $f(\kappa)$ depends on the material properties only and displays the effects of TPA on frequency-comb generation, as far as the threshold is concerned. In the absence of TPA, $f(\kappa = 0) = 1$ and we recover exactly the same mathematical expression for nonlinear ring resonators [48]. On the contrary, in the presence of TPA, $f(\kappa) > 1$ and the minimum power required for comb generation is increased. By substituting Eq. (B2) into Eq. (B1), it is easy to show that the absolute minimum driven intensity to start a comb occurs at the optimal laser detuning

$$\sigma_{\alpha_0}^{\mathrm{th}} = -\frac{\gamma_{\alpha_0}}{2} f(\kappa), \tag{B3}$$

where TPA induces a frequency red shift. Finally, the linear stability analysis of the system at threshold shows the important role of dispersion on the instability of the side-mode perturbations (see Ref. [54]): in order for the cascaded FWM be efficient, the system must be pumped where the dispersion is anomalous, i.e., $d^2\omega/d\alpha^2 > 0$.

[1] P. Del'Haye, A. Schliesser, O. Arcizet, T. Wilken, R. Holzwarth, and T. J. Kippenberg, Optical frequency comb generation from a monolithic microresonator, Nature **450**, 1214 (2007).

[2] Ian Coddington, Nathan Newbury, and William Swann, Dual-comb spectroscopy, Optica **3**, 414 (2016).

[3] Nathalie Picqué and Theodor W. Hänsch, Frequency comb spectroscopy, Nat. Photonics **13**, 146 (2019).

[4] Pablo Marin-Palomo, Juned N. Kemal, Maxim Karpov, Arne Kordts, Joerg Pfeifle, Martin H. P. Pfeiffer, Philipp Trocha, Stefan Wolf, Victor Brasch, Miles H. Anderson, Ralf Rosenberger, Kovendhan Vijayan, Wolfgang Freude, Tobias J. Kippenberg, and Christian Koos, Microresonator-based solitons for massively parallel coherent optical communications, Nature **546**, 274 (2017).

[5] P. Trocha, M. Karpov, D. Ganin, M. H. P. Pfeiffer, A. Kordts, S. Wolf, J. Krockenberger, P. Marin-Palomo, C. Weimann, S. Randel, W. Freude, T. J. Kippenberg, and C. Koos, Ultrafast optical ranging using microresonator soliton frequency combs, Science **359**, 887 (2018).

[6] Daryl T. Spencer *et al.*, An optical-frequency synthesizer using integrated photonics, Nature **557**, 81 (2018).

[7] Andrew J. Benedick, Guoqing Chang, Jonathan R. Birge, Li-Jin Chen, Alexander G. Glenday, Chih-Hao Li, David F. Phillips, Andrew Szentgyorgyi, Sylvain Korzennik, Gabor

Furesz, Ronald L. Walsworth, and Franz X. Kärtner, Visible wavelength astro-comb, Opt. Express **18**, 19175 (2010).

[8] Ewelina Obrzud, Monica Rainer, Avet Harutyunyan, Miles H. Anderson, Junqiu Liu, Michael Geiselmann, Bruno Chazelas, Stefan Kundermann, Steve Lecomte, Massimo Cecconi, Adriano Ghedina, Emilio Molinari, Francesco Pepe, François Wildi, François Bouchy, Tobias J. Kippenberg, and Tobias Herr, A microphotonic astrocomb, Nat. Photonics **13**, 31 (2019).

[9] Ewelina Obrzud, Steve Lecomte, and Tobias Herr, Temporal solitons in microresonators driven by optical pulses, Nat. Photonics **11**, 600 (2017).

[10] T. J. Kippenberg, R. Holzwarth, and S. A. Diddams, Microresonator-based optical frequency combs, Science **29**, 555 (2011).

[11] Tobias J. Kippenberg, Alexander L. Gaeta, Michal Lipson, and Michael L. Gorodetsky, Dissipative Kerr solitons in optical microresonators, Science **361**, 567 (2018).

[12] A. G. Vladimirov, S. V. Gurevich, and M. Tlidi, Effect of Cherenkov radiation on localized-state interaction, Phys. Rev. A **97**, 013816 (2018).

[13] Pedro Parra-Rivas, Damia Gomila, Pere Colet, and Lendert Gelens, Interaction of solitons and the formation of bound states in the generalized Lugiato-Lefever equation, Eur. Phys. J. D **71**, 198 (2017).

[14] Carles Milián, Yaroslav V. Kartashov, Dmitry V. Skryabin, and Lluis Torner, Clusters of Cavity Solitons Bounded by Conical Radiation, Phys. Rev. Lett. **121**, 103903 (2018).

[15] Mengjie Yu, Jae K. Jang, Yoshitomo Okawachi, Austin G. Griffith, Kevin Luke, Steven A. Miller, Xingchen Ji Michal Lipson, and Alexander L. Gaeta, Breather soliton dynamics in microresonators, Nat Commun. **8**, 14569 (2017).

[16] E. Lucas, M. Karpov, H. Guo, M. L. Gorodetsky, and T. J. Kippenberg, Breathing dissipative solitons in optical microresonators, Nat Commun. **8**, 736 (2017).

[17] Hairun Guo, Erwan Lucas, Martin H. P. Pfeiffer, Maxim Karpov, Miles Anderson, Junqiu Liu, Michael Geiselmann, John D. Jost, and Tobias J. Kippenberg, Intermode Breather Solitons in Optical Microresonators, Phys. Rev. X **7**, 041055 (2017).

[18] Daniel C. Cole, Erin S. Lamb, Pascal Del'Haye, Scott A. Diddams, and Scott B. Papp, Soliton crystals in Kerr resonators, Nat. Photonics **11**, 671 (2017).

[19] Maxim Karpov, Martin H. P. Pfeiffer, Hairun Guo, Wenle Weng, Junqiu Liu, and Tobias J. Kippenberg, Dynamics of soliton crystals in optical microresonators, Nat. Phys. **15**, 1071 (2019).

[20] T. Herr, V. Brasch, J. D. Jost, C. Y. Wang, N. M. Kondratiev, M. L. Gorodetsky, and T. J. Kippenberg, Temporal solitons in optical microresonators, Nat. Photonics **8**, 145 (2014).

[21] Alexander L. Gaeta, Michal Lipson, and Tobias J. Kippenberg, Photonic-chip-based frequency combs, Nat. Photonics **13**, 158 (2019).

[22] Stéphane Coen, Hamish G. Randle, Thibaut Sylvestre, and Miro Erkintalo, Modeling of octave-spanning Kerr frequency combs using a generalized mean-field Lugiato-Lefever model, Opt. Lett. **38**, 37 (2013).

[23] C. Milián and D. V. Skryabin, Soliton families and resonant radiation in a micro-ring resonator near zero group-velocity dispersion, Opt. Express **22**, 3732 (2014).

[24] Pedro Parra-Rivas, Damià Gomila, François Leo, Stéphane Coen, and Lendert Gelens, Third-order chromatic dispersion stabilizes Kerr frequency combs, Opt. Lett. **39**, 2971 (2014).

[25] V. Brasch, M. Geiselmann, T. Herr, G. Lihachev, M. H. P. Pfeiffer, M. L. Gorodetsky, and T. J. Kippenberg, Photonic chip–based optical frequency comb using soliton Cherenkov radiation, Science **351**, 357 (2016).

[26] Mark A. Foster, Amy C. Turner, Jay E. Sharping, Bradley S. Schmidt, Michal Lipson, and Alexander L. Gaeta, Broadband optical parametric gain on a silicon photonic chip, Nature **441**, 960 (2006).

[27] Lin Zhang, Chengying Bao, Vivek Singh, Jianwei Mu Changxi Yang, Anuradha M. Agarwal, Lionel C. Kimerling, and Jurgen Michel, Generation of two-cycle pulses and octave-spanning frequency combs in a dispersion-flattened micro-resonator, Opt. Lett. **38**, 5122 (2013).

[28] Yoshitomo Okawachi, Michael R. E. Lamont, Kevin Luke, Daniel O. Carvalho, Mengjie Yu Michal Lipson, and Alexander L. Gaeta, Bandwidth shaping of microresonator-based frequency combs via dispersion engineering, Opt. Lett. **39**, 3535 (2014).

[29] Ivan S. Grudinin and Nan Yu, Dispersion engineering of crystalline resonators via microstructuring, Optica **2**, 221 (2015).

[30] Daniel C. Cole, Alessandra Gatti, Scott B. Papp, Franco Prati, and Luigi Lugiato, Theory of Kerr frequency combs in Fabry-Perot resonators, Phys. Rev. A **98**, 013831 (2018).

[31] Su-Peng Yu Hojoong Jung, Travis C. Briles, Srinivasan Kartik, and Scott B. Papp, Photonic-crystal-reflector nanoresonators for Kerr-frequency combs, arXiv:1904.07289.

[32] Amnon Yariv, Yong Xu, Reginald K. Lee, and Axel Scherer, Coupled-resonator optical waveguide: A proposal and analysis, Opt. Lett. **24**, 711 (1999).

[33] Marin Soljačić, Steven G. Johnson, Shanhui Fan, Mihai Ibanescu, Erich Ippen, and J. D. Joannopoulos, Photonic-crystal slow-light enhancement of nonlinear phase sensitivity, J. Opt. Soc. Am. B **19**, 2052 (2002).

[34] Yan Chen and Steve Blair, Nonlinearity enhancement in finite coupled-resonator slow-light waveguides, Opt. Express **12**, 3353 (2004).

[35] D. O'Brien, M. D. Settle, T. Karle, A. Michaeli, M. Salib, and T. F. Krauss, Coupled photonic crystal heterostructure nanocavities, Opt. Express **15**, 1228 (2007).

[36] Masaya Notomi, Eiichi Kuramochi, and Takasumi Tanabe, Large-scale arrays of ultrahigh-q coupled nanocavities, Nat. Photonics **2**, 741 (2008).

[37] Nobuyuki Matsuda, Takumi Kato, Ken-ichi Harada, Hiroki Takesue, Eiichi Kuramochi, Hideaki Taniyama, and Masaya Notomi, Slow light enhanced optical nonlinearity in a silicon photonic crystal coupled-resonator optical waveguide, Opt. Express **19**, 19861 (2011).

[38] Momchil Minkov and Vincenzo Savona, Wide-band slow light in compact photonic crystal coupled-cavity waveguides, Optica **2**, 631 (2015).

[39] Yiming Lai, Mohamed Sabry Mohamed, Boshen Gao, Momchil Minkov, Robert W. Boyd, Vincenzo Savona, Romuald Houdré, and Antonio Badolato, Ultra-wide-band structural slow light, Sci. Rep. **8**, 14811 (2018).

[40] Mohamed Sabry Mohamed, Yiming Lai, Momchil Minkov, Vincenzo Savona, Antonio Badolato, and Romuald Houdré, Influence of disorder and finite-size effects on slow light transport in extended photonic crystal coupled-cavity waveguides, ACS Photonics **5**, 4846 (2018).

[41] Lucio Claudio Andreani and Dario Gerace, Photonic-crystal slabs with a triangular lattice of triangular holes investigated using a guided-mode expansion method, Phys. Rev. B **73**, 235114 (2006).

[42] LUMERICAL, commercial software developed by Lumerical Solutions, Inc. (2019, http://www.lumerical.com).

[43] Weiwei Song, Ryan A. Integlia, and Wei Jiang, Slow light loss due to roughness in photonic crystal waveguides: An analytic approach, Phys. Rev. B **82**, 235306 (2010).

[44] Nick K. Hon, Richard Soref, and Bahram Jalali, The third-order nonlinear optical coefficients of Si, Ge, and $Si_{1-x}Ge_x$ in the midwave and longwave infrared, J. Appl. Phys. **110**, 011301 (2011).

[45] Yao Zhang and Baojun Li, Photonic crystal-based bending waveguides for optical interconnections, Opt. Express **14**, 5723 (2006).

[46] Yanne K. Chembo, Quantum dynamics of Kerr optical frequency combs below and above threshold: Spontaneous four-wave mixing, entanglement, and squeezed states of light, Phys. Rev. A **93**, 033820 (2016).

[47] Yanne K. Chembo, Dmitry V. Strekalov, and Nan Yu, Spectrum and Dynamics of Optical Frequency Combs Generated with Monolithic Whispering Gallery Mode Resonators, Phys. Rev. Lett. **104**, 103902 (2010).

[48] Yanne K. Chembo and Nan Yu, Modal expansion approach to optical-frequency-comb generation with monolithic whispering-gallery-mode resonators, Phys. Rev. A **82**, 033801 (2010).

[49] Yanne K. Chembo and Curtis R. Menyuk, Spatiotemporal Lugiato-Lefever formalism for Kerr-comb generation in whispering-gallery-mode resonators, Phys. Rev. A **87**, 053852 (2013).

[50] Ryan K. W. Lau, Michael R. E. Lamont, Yoshitomo Okawachi, and Alexander L. Gaeta, Effects of multiphoton absorption on parametric comb generation in silicon microresonators, Opt. Lett. **40**, 2778 (2015).

[51] Ambaresh Sahoo, Samudra Roy, and Govind P. Agrawal, Perturbed dissipative solitons: A variational approach, Phys. Rev. A **96**, 013838 (2017).

[52] T. Herr, K. Hartinger, J. Riemensberger, C. Y. Wang, E. Gavartin, R. Holzwarth, M. L. Gorodetsky, and T. J. Kippenberg, Universal formation dynamics and noise of Kerr-frequency combs in microresonators, Nat. Photonics **6**, 480 (2012).

[53] T. Hansson, D. Modotto, and S. Wabnitz, On the numerical simulation of Kerr frequency combs using coupled mode equations, Opt. Commun. **312**, 134 (2014).

[54] See the Supplemental Material at http://link.aps.org/supplemental/10.1103/PhysRevApplied.12.064065 for full details of the mathematical derivations and soliton dynamics.

[55] Cyril Godey, Irina V. Balakireva, Aurélien Coillet, and Yanne K. Chembo, Stability analysis of the spatiotemporal Lugiato-Lefever model for Kerr optical frequency combs in the anomalous and normal dispersion regimes, Phys. Rev. A **89**, 063814 (2014).

[56] Myoung-Gyun Suh and Kerry Vahala, Gigahertz-repetition-rate soliton microcombs, Optica **5**, 65 (2018).

[57] Philip Trøst Kristensen and Stephen Hughes, Modes and mode volumes of leaky optical cavities and plasmonic nanoresonators, ACS Photonics **1**, 2 (2014).

[58] John D. Joannopoulos, Steven G. Johnson, Joshua N. Winn, and Robert D. Meade *Photonic Crystals: Molding the Flow of Light* (Princeton University Press, Princeton, 2008), 2nd ed., Chap. 2–3.

[59] Robert W. Boyd, *Nonlinear Optics* (Academic Press, Rochester, 2007), 3rd ed.

[60] Pierre Colman, Field renormalization in photonic crystal waveguides, Phys. Rev. A **92**, 013827 (2015).